Open Transmission Channels in Multimode Fiber Cavities with Random Mode Mixing

Guy Pelc,[1] Shay Guterman,[1] Rodrigo Gutiérrez-Cuevas,[2] Arthur Goetschy,[2] Sébastien M. Popoff,[2] and Yaron Bromberg[1,*]

[1]Racah Institute of Physics, The Hebrew University of Jerusalem, Jerusalem 91904, Israel
[2]Institut Langevin, ESPCI Paris, PSL University, CNRS, Paris 75005, France

(Received 11 February 2025; revised 14 August 2025; accepted 12 September 2025; published 21 October 2025)

The transport of light in disordered media is governed by open transmission channels, which enable nearly complete transmission of the incident power, despite low average transmission. Extensively studied in diffusive media and chaotic cavities, open channels exhibit unique properties such as universal spatial structure and extended dwell times. However, their experimental study is challenging due to the large number of modes required for control and measurement. We propose a multimode fiber cavity (MMFC) as a platform to explore open channels. Leveraging mode confinement and finite angular spread, MMFCs enabled full channel control, yielding an 18-fold power enhancement in experiment by selectively exciting an open channel with a transmission of 0.90 ± 0.04. By analyzing 100 transmission matrices of MMFC realizations, we observed a bimodal transmission eigenvalue distribution, indicating high channel control and low losses. The scalability of MMFCs, combined with long dwell times and potential for nonlinear phenomena, offers new opportunities for studying complex wave transport.

DOI: 10.1103/fvvb-76nn

When coherent light illuminates thick scattering samples, most of the incident power is backscattered. However, theory predicts that, with a sufficiently large illumination area, one can identify an incident wave front that enables all light to be transmitted through the sample via the so-called open transmission channels [1,2]. Advances in wave front shaping have allowed precise control over optical wave fronts [3–5], enabling the selective excitation of open channels [6,7]. Over the past decade, several unique properties of open channels have been uncovered, including correspondence with quasinormal modes [8–11], universal spatial structure [7,12–16], and association with extended dwell times inside the sample [10,17,18].

Increased dwell times in disordered samples enhance light-matter interactions, boost nonlinear effects, and improve environmental sensitivity, key features for sensing applications. Thus, studying the existence of open channels in systems relevant to sensing and nonlinear optics, such as optical fibers, is desirable.

Owing to the similarity between transmission through multimode fibers and scattering samples, analogies between these systems have been extensively explored over the past decade, particularly in the context of speckle statistics and wave front shaping [19–22]. A key advantage of multimode fibers is that all their modes can be controlled using a spatial light modulator (SLM) [23,24]. In standard optical fibers, all channels transmit light completely. However, by introducing reflective coatings to create a multimode fiber cavity (MMFC), most incident light is backreflected, and the concept of open channels becomes applicable. Without mode mixing, an open channel of an MMFC simply corresponds to a guided mode whose propagation constant matches the Fabry-Pérot resonance condition. However, in the presence of strong mode mixing, the existence and properties of open channels are more intricate.

In this Letter, we demonstrate that MMFCs with strong mode mixing can indeed support open channels. We show that, despite strong coupling between guided modes, it is possible to selectively excite an open channel and achieve an 18-fold enhancement in transmitted power through the cavity. We find that the transmission eigenvalue distribution is bimodal, reflecting the high control of MMFC channels and its minimal losses. These findings establish MMFCs as a versatile platform for studying and controlling complex optical modes extending beyond open channels, such as recently discovered reflectionless scattering modes [25,26].

Open channels are found by measuring the transmission matrix of the sample T, which relates the input and output fields by $\vec{\psi}_{\text{out}} = T\vec{\psi}_{\text{in}}$ [27]. The singular value decomposition of T, or equivalently, the eigenvectors of the Hermitian matrix $T^\dagger T$, define the transmission eigenchannels of the sample $T^\dagger T\vec{v}_n = \tau_n \vec{v}_n$, where the eigenvalues τ_n correspond to the transmission coefficients. To selectively excite the most open channel, the wave front of the input field is tailored to match the wave front corresponding to the eigenchannel $\vec{v}_1$ with the highest transmission coefficient τ_1. The two key ingredients for realizing open channels are, therefore, coherent detection of the light

*Contact author: yaron.bromberg@mail.huji.ac.il

transmitted through the fiber and precise control over the amplitude and phase of the incident wave front.

To experimentally study the transmission eigenchannels of an MMFC, we used a 1 m long step-index fiber with a core diameter of 25 μm and a numerical aperture of NA = 0.1, coated with reflective coatings with reflectivity $\rho = 0.88$. We placed the MMFC in one arm of a Mach-Zehnder interferometer [Figs. 1(a) and S1]. A tunable laser ($\lambda = 632$ nm) with a long coherence length (> 100 m) enabled interference of multiple round trips in the cavity. The amplitude and phase of the incident field were tailored using a phase-only SLM in combination with a spatial filter for amplitude modulation [28] (see Supplemental Material, Sec. A [29]). The transmitted field interfered with a reference beam in an off-axis holography configuration, and both output polarizations were imaged onto a camera. We normalized the reconstructed output field so that its total power matched the output power measured by a calibrated photodiode monitoring the transmitted light (see Supplemental Material, Fig. S1 and Sec. B [29]).

We measured the MMFC's transmission matrix T by illuminating the fiber core with a set of 242 tilted beams (121 per input polarization). The tilts were generated by applying equally spaced linear phase ramps on the SLM, spanning the angular bandwidth defined by the NA of the fiber. For each input, the fields of the two output polarizations were rearranged into a one-dimensional vector, comprising one column of the transmission matrix. To compensate for thermal drifts, we adjusted the laser wavelength by a few femtometers after every 10 input modes (see Supplemental Material, Sec. A, for further details on the transmission matrix measurement [29]). The decomposition of the transmission matrix into the fiber mode basis is depicted in Fig. 1(b), exhibiting strong mode mixing with 0.8 of the energy located in the off-diagonal elements (see Supplemental Material, Sec. C for details on the fiber mode decomposition [29]).

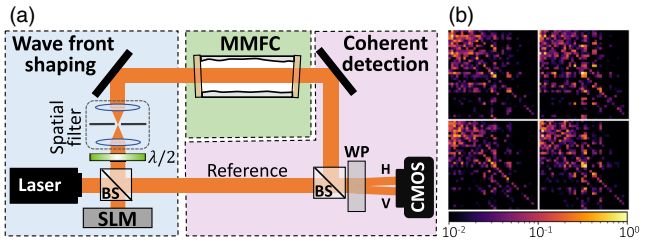

FIG. 1. Schematic of the experimental setup and measured transmission matrix. (a) The transmission matrix of the multimode fiber cavity (MMFC) is measured by placing it in one arm of a Mach-Zehnder interferometer. The polarization-dependent complex field at the output of the fiber is measured for a set of input modes excited using the SLM. The wave front required to excite an open channel is computed from the transmission matrix and then realized using the wave front shaping apparatus. A spatial filter is used to convert the phase-only SLM to an amplitude and phase modulator. A half-wave plate ($\lambda/2$) is used to control the input polarization, while a Wollaston prism (WP) before the camera (CMOS) separates horizontal (H) and vertical (V) polarizations. BS: beam splitter. (b) The absolute value squared of a measured transmission matrix, presented in the fiber mode basis, exhibiting strong mode mixing. The left (right) quadrants correspond to measurements in the horizontal (vertical) input polarizations, while the top (bottom) quadrants correspond to measurements in the horizontal (vertical) output polarizations. In each quadrant, 0.8 of the energy is concentrated in the off-diagonal elements.

The eigenvalues obtained by diagonalizing $T^\dagger T$ are presented in Fig. 2. We observed that $N_{\text{open}} = 4$ channels exhibit transmission coefficients higher than $\tau_c = (1 + \pi^2/4)^{-1} \approx 0.288$, a threshold of order unity that we use to define an open channel in MMFCs (see Supplemental Material, Sec. G1 [29]). A noticeable gap at the 67th transmission coefficient suggests that the MMFC supports $N = 67$ modes. This is largely consistent with the measured transmission matrix of the fiber without reflective coatings, which exhibits 34 guided modes and two leaky modes per polarization (see Supplemental Material, Sec. E [29]). The average transmission, calculated as the mean of the first 67 transmission coefficients, is $\langle\tau\rangle = 0.065 \pm 0.001$. The optical conductance, defined as the product of the average transmission and the number of channels, is $g = N\langle\tau\rangle \approx 4.3$. This value is close to the number of open channels we observed, in agreement with the threshold τ_c used to define open channels (see Supplemental Material, Sec. G1 [29]).

The transmission properties of the MMFC are governed by the statistics of the transmission coefficients, particularly

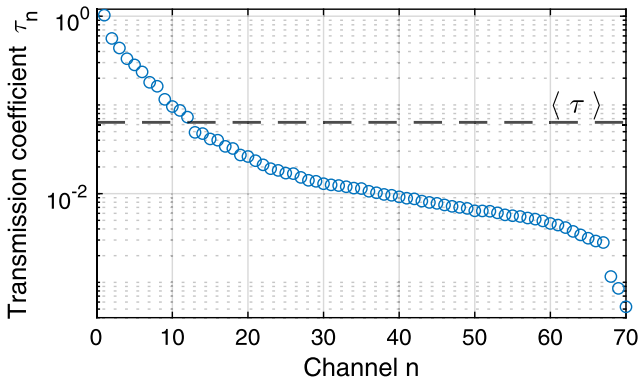

FIG. 2. Transmission coefficients τ_n obtained by diagonalizing $T^\dagger T$ for an experimentally measured transmission matrix T. Four open channels with transmission coefficients higher than $\tau_c = 0.288$ are observed. Only the 70 most significant transmission coefficients are presented. The noticeable gap between channels 67 and 68 indicates that the MMFC supports 67 guided modes. The dashed horizontal line marks the average transmission $\langle\tau\rangle = 0.065 \pm 0.001$. The small gap between τ_1 and τ_2 points to a small offset in the off-axis reconstruction of the complex field, most likely arising from inhomogeneities in the reference beam. The uncertainties are on the order of 1%, smaller than the marker size (see Supplemental Material, Sec. D [29]).

their probability density function (PDF) f_τ. For diffusive samples, the PDF exhibits a bimodal shape with peaks at $\tau = 0$ and $\tau = 1$ [36]. Observing this bimodal distribution requires near-complete control over all channels. With only partial control, the transmission matrix elements become uncorrelated, and the PDF converges to the Marčenko-Pastur distribution, which is bounded by a maximal transmission coefficient of $4\langle\tau\rangle$ [27,37]. The fact that we observed four open channels with transmissions exceeding this bound indicates that we had sufficient control to measure a transmission matrix with correlated elements, resulting in a PDF that deviates from the Marčenko-Pastur distribution. Nevertheless, to test whether our degree of control is sufficient to resolve the intrinsic PDF of the MMFC, we measured it directly.

To obtain the PDF experimentally, we measured multiple realizations of the MMFC's transmission matrix by leveraging its spectral sensitivity. Specifically, we recorded 100 transmission matrices at wavelengths spaced by 20 fm, exceeding the MMFC's spectral correlation width of ≈10 fm (see Supplemental Material, Sec. F and Fig. S3 [29]). Over this wavelength span, the change in the fiber's V number is on the order of 10^{-6}; thus, the number of guided modes remains unchanged, and the changes in their spatial profiles are negligible. For each matrix, we computed the transmission coefficients and constructed their histogram (Fig. 3). The resulting PDF remains finite at $\tau \approx 1$ ($f_\tau \approx 10^{-2}$), reflecting a nonzero probability of obtaining open channels with nearly unit transmission.

To further analyze the measured distribution of the transmission coefficients, we modeled the transmission through the MMFC as interference of multiple round trips within the cavity. Each round trip can be represented by $\hat{r}_1 T_0^{\mathsf{T}} \hat{r}_2 T_0$, where T_0 and T_0^{T} represent the transmission matrix of an uncoated fiber and its transpose, respectively, and the matrices $\hat{r}_{i=1,2}$ describe reflection from the two facets of the fiber [Fig. 4(a)]. Analogously to a Fabry-Pérot cavity, the total transmission matrix of the MMFC is given by the infinite series of round trip contributions (for additional details, see Supplemental Material, Sec. G1 [29]):

$$T = \hat{t}_2 \frac{1}{1 - T_0 \hat{r}_1 T_0^{\mathsf{T}} \hat{r}_2} T_0 \hat{t}_1, \tag{1}$$

where $\hat{t}_{i=1,2}$ represents the transmission matrices through the coated facets of the MMFC. When the facets are perfectly orthogonal to the propagation axis of the fiber, the reflection and transmission matrices of the facets remain diagonal in the fiber mode basis $\hat{r}_i = \sqrt{\rho_i}\mathbb{1}$, $\hat{t}_i = \sqrt{1-\rho_i}\mathbb{1}$. However, slight facet angles, often present in connectorized fibers [38], introduce coupling between the modes,

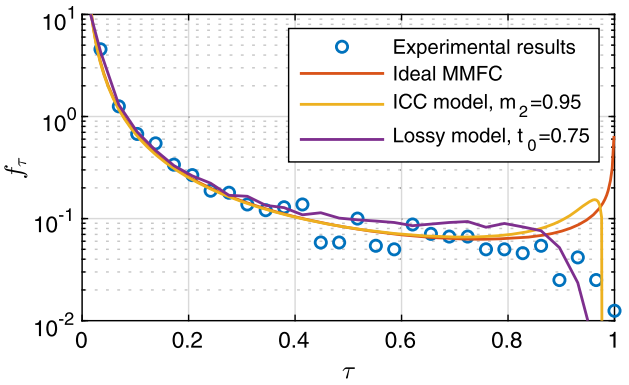

FIG. 3. The probability density function (PDF) of the transmission coefficients, f_τ, was obtained from the histogram of the transmission coefficients of an ensemble of 100 matrices. The experimental data (circles) are compared to the expected distribution of an ideal MMFC (red line), the incomplete channel control (ICC) model (orange line), and the lossy model (purple line). The measured data follow the ideal distribution for $\tau \lesssim 0.8$ and then gradually decay, reaching $\tau = 1$ with a finite probability. Comparison to the ICC model, which assumes full control over the input modes and control over $m_2 = 0.95$ of the output modes, demonstrates that the MMFC provides a high degree of control over both input and output modes. Additionally, comparison to the lossy model, which assumes that the four highest-order modes experience transmission of $t_0 = 0.75$ while all other modes do not experience loss, suggests that coupling to a few leaky modes can explain the deviation of the measured data from the ideal MMFC model.

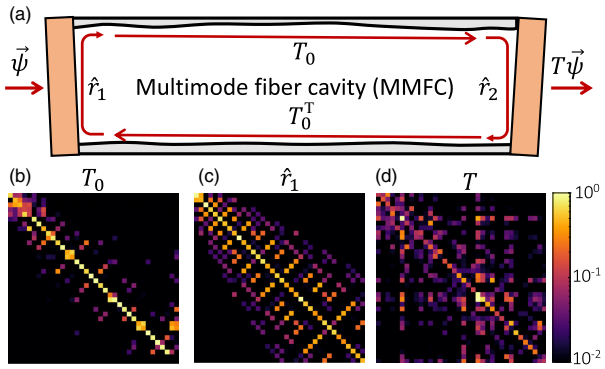

FIG. 4. Transmission matrix and mode mixing in an MMFC. (a) Schematic of the MMFC. Each round trip is described by $\hat{r}_1 T_0^{\mathsf{T}} \hat{r}_2 T_0$, where T_0 and T_0^{T} are the transmission matrix of an uncoated fiber and its transpose, respectively, and $\hat{r}_1, \hat{r}_2$ denote the matrices describing the reflection from the facets. (b) Typical measured transmission matrix T_0 of a 1 m long uncoated step-index fiber supporting $N = 34$ modes per polarization. The matrix exhibits weak mode mixing, with 0.8 of the energy concentrated in the diagonal blocks of the degenerate modes. (c) Numerically computed reflection matrix $\hat{r}_1$, assuming a facet angle of $\theta = 5 \times 10^{-3}$ rad, obtained by decomposing a linear phase tilt into the fiber modes. (d) Computed transmission matrix of the MMFC using Eq. (1), for T_0 from (b) and $\hat{r}_i$ from (c). All matrices depict the absolute value squared of one polarization quadrant of the full transmission matrix.

manifested by nondiagonal reflection matrices with mean reflectivity ρ_i [Fig. 4(c)].

Measurements of the transmission matrix T_0 for an uncoated fiber exhibit weak mode mixing, with only 0.2 of the energy concentrated in the off-diagonal elements of the matrix [Fig. 4(b)]. In contrast, the measured transmission matrix of the MMFC shows strong mode mixing, with 0.8 of the energy in the off-diagonal elements [Fig. 1(b)]. To investigate the origin of the higher mode mixing, we plugged into Eq. (1) the measured transmission matrix T_0, where we eliminated the effect of mode-dependent loss associated with measurement of T_0 by setting its singular values to unity. This computation yields a transmission matrix with 0.5 of the energy in the off-diagonal elements. By introducing to the model a slight tilt of the fiber facets, the mode mixing is further increased. For typical tilt angles obtained in optical fibers ($\theta = 5 \times 10^{-3}$) [38], mode mixing increased significantly, with 0.7 of the energy in off-diagonal elements [Fig. 4(d)].

Using the model described by Eq. (1), incorporating mode mixing from tilted facets, we computed analytically the PDF of the transmission coefficients within the framework of random matrix theory (see Supplemental Material, Sec. G1 [29]). As in scattering samples, it exhibits a bimodal distribution (Fig. 3, red curve), where the exact form of the PDF depends on the coating reflectivity. For the experimental reflectivity $\rho = 0.88$, the measured PDF follows the MMFC model up to transmission values of $\tau \sim 0.8$.

The slight deviation between measured and model PDFs can be used to estimate the MMFC channel control, as incomplete wave front control or losses typically reduce the number of open channels. In contrast, mode mixing alone does not affect the transmission eigenvalue distribution, as it corresponds to unitary transformations that preserve the eigenvalues of $T^\dagger T$ (see Supplemental Material, Sec. G1 [29]).

We, therefore, considered two simplified single-parameter models. In the incomplete channel control (ICC) model, we assumed a lossless MMFC, while allowing for an incomplete measurement of its transmission matrix (see Supplemental Material, Sec. G2 [29] and Ref. [37]). The best agreement between the ICC model and the experimental data was obtained by assuming full control over all incident channels and 95% control over the output channels (Fig. 3, orange curve). In the loss model, we assumed the MMFC is lossy due to leaky fiber modes but that its transmission matrix was perfectly measured (see Supplemental Material, Sec. G3 [29]). Consistency with the experimental data was achieved by assuming that the four highest-order modes of the fiber were leaky modes with a transmission of $t_0 = 0.75$, corresponding to an average loss of less than 0.015 per channel (Fig. 3, purple curve). This assumption aligned with a direct measurement of the transmission matrix of a similar fiber without reflective coatings (see Supplemental Material, Sec. E [29]). Neither model perfectly fits the data, but both suggest high channel control and low overall loss.

In scattering media, open transmission eigenchannels exhibit significantly longer dwell times compared to the average value [10,17,18,39]. To investigate whether this property of open channels also holds in MMFCs, we performed numerical simulations of light propagation in our MMFC setup and computed the expectation values of the dwell time operator, $Q = -i[T^\dagger(dT/d\omega) + R^\dagger(dR/d\omega)]$, where R is the reflection matrix of the MMFC [18] (see Supplementary Material Sec. H [29] for details). The computation reveals that the dwell time of the open channel (110 ns) exceeds the mean dwell time (7 ns) by more than an order of magnitude and that the dwell time of transmission eigenchannels increases monotonically with their transmission coefficients (see Fig. S6).

The MMFC platform's high control enables selective excitation of transmission eigenchannels and study of their spatial structure. To excite an open channel of the system, we tailored the incident wave front to match the input $\vec{v}_1$ that corresponds to the channel with $\tau_1 \approx 1$ shown in Fig. 2. Since mode mixing in the MMFC is polarization-dependent [see Fig. 1(b)], the incident field corresponding to $\vec{v}_1$ consisted of two different polarization components. However, as the SLM can shape only one polarization at a time, we first sent the horizontal polarization component $\vec{v}_1$ into the fiber and measured the output field $\vec{\psi}_{1,H}$. At the output, both polarization components were measured simultaneously, so $\vec{\psi}_{1,H}$ includes both components, with the subscript H indicating the input polarization. Next, we rotated the input polarization state by 90°, sent the vertical component of $\vec{v}_1$, and measured the output field $\vec{\psi}_{1,V}$. Finally, we coherently combined the measured output fields to obtain the total output field for simultaneous excitation of both input polarizations: $\vec{\psi}_1 = \vec{\psi}_{1,H} + \vec{\psi}_{1,V}$, as depicted in Fig. 5.

To directly measure the transmission coefficient of the excited open channel, we normalized the total output power, $\|\vec{\psi}_{1,H} + \vec{\psi}_{1,V}\|^2$, by the total input power $p_H + p_V$, measured with a calibrated photodetector monitoring the input beam before entering the MMFC (see Fig. S1 [29]). We denote the transmissions measured directly from the ratio of output and input powers by $\tilde{\tau}_n$, to distinguish them from the transmission coefficients τ_n computed from the singular value decomposition of the measured transmission matrix. The measured transmission coefficient is given by $\tilde{\tau}_1 = \|\vec{\psi}_{1,H} + \vec{\psi}_{1,V}\|^2/(p_H + p_V)$. For the open channel depicted in Fig. 5, we obtained $\tilde{\tau}_1 = 0.90 \pm 0.04$, representing an 18-fold enhancement compared to the average transmission $\langle\tilde{\tau}\rangle = 0.049 \pm 0.001$ measured for a set of random inputs. The measured transmission $\tilde{\tau}_1$ is about 10% lower than the transmission coefficient τ_1 computed from the transmission matrix, but the 18-fold enhancement relative to the average intensity remains consistent in both cases. This discrepancy likely arises

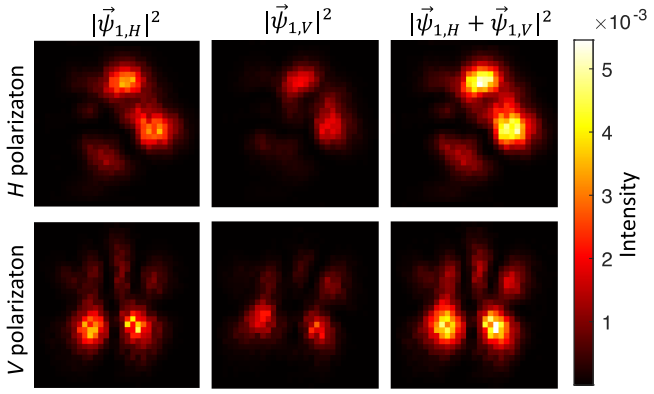

FIG. 5. Selective excitation of the highest transmission channel. The first transmission eigenchannel $\vec{v}_1$ was decomposed into its two input polarization components, $\vec{v}_{1,H}$ and $\vec{v}_{1,V}$, which were excited sequentially. The left column shows the measured output intensity, $|\vec{\psi}_{1,H}(x,y)|^2$, for excitation of the horizontal component, while the central column shows the output intensity, $|\vec{\psi}_{1,V}(x,y)|^2$, for excitation of the vertical component. The right column depicts the intensity for the coherent superposition, $|\vec{\psi}_{1,H}(x,y)+\vec{\psi}_{1,V}(x,y)|^2$. The top row represents the horizontal polarization component of the output, and the bottom row represents the vertical polarization component. The output intensity patterns were normalized by the power measured at the input of the MMFC, ensuring that the sum over all pixels corresponds to the transmission of the pattern. The transmissions for $\vec{\psi}_{1,H}$, $\vec{\psi}_{1,V}$, and $\vec{\psi}=\vec{\psi}_{1,H}+\vec{\psi}_{1,V}$ are $\tilde{\tau}_{1,H}=0.60$, $\tilde{\tau}_{1,V}=0.35$, and $\tilde{\tau}_1=0.90$, respectively.

from inaccuracies in the transmission matrix measurement and phase instabilities.

Figure 5 shows that the spatial distribution of the output fields $\vec{\psi}_{1,H}$ and $\vec{\psi}_{1,V}$ are highly correlated, despite their orthogonal input polarizations. This spatial overlap enables efficient constructive interference, which is required for open channels with near-unity transmission coefficients. Similarly, multiple round trips in the cavity are expected to interfere constructively at the fiber output. In a perfect fiber without mode mixing, guided modes maintain their transverse shape, and open channels correspond to the guided modes whose propagation constants satisfy constructive interference at the output of the fiber. However, in the presence of mode mixing, none of the modes retain their transverse shape preventing good spatial overlap of multiple round trips. Indeed, when we coupled the guided modes of the fiber (LP_{lm}) to the MMFC, the highest transmission we observed was $\tilde{\tau}_{LP}=0.17$, far below $\tilde{\tau}_1$. MMFC open channels uniquely retain transverse shape across round trips despite mode mixing (see Supplemental Material, Sec. G1 [29]). While we cannot directly probe the transverse shape after each round trip, we observed indirect evidence of this feature by tuning the wavelength of the laser by a few femtometers. For open channels, the intensity quickly dropped, while the transverse shape remained unchanged. The fact that the output intensity pattern did not vary indicates that the wavelength detuning was too small to significantly change the relative phases of the transverse modes. Thus, only the global phase accumulated over different round trips can affect the total output intensity. This behavior is analogous to that of Fabry-Pérot cavities, where wavelength detuning alters the relative phase between successive round trips.

In this Letter, we investigated open channels and their distribution in MMFCs. By selectively exciting an open channel, we achieved a transmission of $\tilde{\tau}_1=0.90\pm0.04$, corresponding to an 18-fold enhancement over the measured average transmission $\langle\tilde{\tau}\rangle=0.049\pm0.001$. To gather statistical insights, we measured multiple transmission matrices at different wavelengths and extracted the PDF of the transmission coefficients. The obtained PDF exhibited a nonzero probability of channels with $\tau=1$, though slightly lower than predicted by the ideal bimodal distribution. This deviation allowed us to estimate the degree of control and loss in our system, suggesting that we controlled over 0.95 of the MMFC modes.

MMFCs enable high control by confining channels with a finite angular spread, making them easily addressable with an SLM. This control revealed strong correlations between orthogonal input polarizations in near-unit transmission channels, highlighting their origin in optimal constructive interference and long dwell times.

MMFCs offer exceptional scalability, with the number of channels readily extendable to thousands by increasing the core size and numerical aperture. This scalability, combined with long dwell times, compatibility with extended fiber lengths, and strong confinement that enables operation in the nonlinear regime, positions MMFCs as a powerful platform for studying wave transport and nonlinear dynamics in complex media. In addition, the long dwell times of the MMFC transmission channels and their sensitivity to the fiber's conformation and surroundings suggest that MMFCs could also be valuable for developing advanced fiber based sensing schemes, including multiparameter sensing, for example, in fiber cavity ring-down spectroscopy [40,41].

Acknowledgments—We wish to thank Hui Cao and Valentin Freilikher for insightful and fruitful discussions. Y. B. acknowledges support from Israeli Science Foundation Grants No. 1268/16 and No. 2497/21, and the Zuckerman STEM Leadership Program. A. G. and S. M. P. acknowledge support by the program "Investissements d'Avenir" launched by the French Government.

Data availability—The data that support the findings of this article are not publicly available upon publication because it is not technically feasible and/or the cost of preparing, depositing, and hosting the data would be prohibitive within the terms of this research project. The data are available from the authors upon reasonable request.

[1] O. Dorokhov, Solid State Commun. **51**, 381 (1984).
[2] J. Pendry, A. MacKinnon, and A. Pretre, Physica (Amsterdam) **168A**, 400 (1990).
[3] I. M. Vellekoop and A. Mosk, Opt. Lett. **32**, 2309 (2007).
[4] I. M. Vellekoop and A. P. Mosk, Phys. Rev. Lett. **101**, 120601 (2008).
[5] M. Mounaix, N. K. Fontaine, D. T. Neilson, R. Ryf, H. Chen, J. C. Alvarado-Zacarias, and J. Carpenter, Nat. Commun. **11**, 5813 (2020).
[6] R. Sarma, A. G. Yamilov, S. Petrenko, Y. Bromberg, and H. Cao, Phys. Rev. Lett. **117**, 086803 (2016).
[7] N. Bender, A. Yamilov, H. Yılmaz, and H. Cao, Phys. Rev. Lett. **125**, 165901 (2020).
[8] J. Wang and A. Z. Genack, Nature (London) **471**, 345 (2011).
[9] A. Peña, A. Girschik, F. Libisch, S. Rotter, and A. Chabanov, Nat. Commun. **5**, 3488 (2014).
[10] M. Davy, Z. Shi, J. Wang, X. Cheng, and A. Z. Genack, Phys. Rev. Lett. **114**, 033901 (2015).
[11] M. Davy and A. Z. Genack, Nat. Commun. **9**, 4714 (2018).
[12] W. Choi, A. P. Mosk, Q.-Han Park, and W. Choi, Phys. Rev. B **83**, 134207 (2011).
[13] M. Davy, Z. Shi, J. Park, C. Tian, and A. Z. Genack, Nat. Commun. **6**, 6893 (2015).
[14] O. S. Ojambati, H. Yılmaz, A. Lagendijk, A. P. Mosk, and W. L. Vos, New J. Phys. **18**, 043032 (2016).
[15] H. Yılmaz, C. W. Hsu, A. Yamilov, and H. Cao, Nat. Photonics **13**, 352 (2019).
[16] A. Z. Genack, Y. Huang, A. Maor, and Z. Shi, Nat. Commun. **15**, 2606 (2024).
[17] Z. Shi, M. Davy, and A. Z. Genack, Opt. Express **23**, 12293 (2015).
[18] M. Durand, S. M. Popoff, R. Carminati, and A. Goetschy, Phys. Rev. Lett. **123**, 243901 (2019).
[19] H. Cao, T. Čižmár, S. Turtaev, T. Tyc, and S. Rotter, Adv. Opt. Photonics **15**, 524 (2023).
[20] Y. Bromberg, B. Redding, S. M. Popoff, and H. Cao, Phys. Rev. A **93**, 023826 (2016).
[21] S. Li, S. A. Horsley, T. Tyc, T. Čižmár, and D. B. Phillips, Nat. Commun. **12**, 3751 (2021).
[22] R. Gutiérrez-Cuevas, A. Goetschy, Y. Bromberg, G. Pelc, E. R. Andresen, L. Bigot, Y. Quiquempois, M. Bsaibes, P. Sillard, M. Bigot *et al.*, Phys. Rev. X **14**, 031046 (2024).
[23] M. Mounaix and J. Carpenter, Nat. Commun. **10**, 5085 (2019).
[24] H. Kupianskyi, S. A. Horsley, and D. B. Phillips, Optica **11**, 101 (2024).
[25] J. Sol, A. Alhulaymi, A. D. Stone, and P. Del Hougne, Sci. Adv. **9**, eadf0323 (2023).
[26] X. Jiang, S. Yin, H. Li, J. Quan, H. Goh, M. Cotrufo, J. Kullig, J. Wiersig, and A. Alù, Nat. Phys. **20**, 109 (2024).
[27] S. M. Popoff, G. Lerosey, R. Carminati, M. Fink, A. C. Boccara, and S. Gigan, Phys. Rev. Lett. **104**, 100601 (2010).
[28] V. Arrizón, U. Ruiz, R. Carrada, and L. A. González, J. Opt. Soc. Am. A **24**, 3500 (2007).
[29] See Supplemental Material at http://link.aps.org/supplemental/10.1103/fvvb-76nn for details, which includes Refs. [30–35].
[30] P. Pai, J. Bosch, and A. P. Mosk, OSA Continuum **3**, 637 (2020).
[31] M. Plöschner, T. Tyc, and T. Čižmár, Nat. Photonics **9**, 529 (2015).
[32] M. W. Matthès, P. del Hougne, J. de Rosny, G. Lerosey, and S. M. Popoff, Optica **6**, 465 (2019).
[33] J. A. Melsen and C. W. J. Beenakker, Phys. Rev. B **51**, 14483 (1995).
[34] Y. Imry, Europhys. Lett. **1**, 249 (1986).
[35] P. Lalanne, W. Yan, K. Vynck, C. Sauvan, and J.-P. Hugonin, Laser Photonics Rev. **12**, 1700113 (2018).
[36] C. W. J. Beenakker, Rev. Mod. Phys. **69**, 731 (1997).
[37] A. Goetschy and A. D. Stone, Phys. Rev. Lett. **111**, 063901 (2013).
[38] Senko Advanced Components, Key errors and apex offset: Causes and solutions for fiber optic networks, Application Note (2022), available at https://www.senko.com/wp-content/uploads/2021/09/Key-Errors-and-Apex-Offset-02142022.pdf (Accessed: January 15, 2025).
[39] S. Rotter and S. Gigan, Rev. Mod. Phys. **89**, 015005 (2017).
[40] H. Waechter, J. Litman, A. H. Cheung, J. A. Barnes, and H.-P. Loock, Sensors **10**, 1716 (2010).
[41] M. Fabian, E. Lewis, T. Newe, and S. Lochmann, Meas. Sci. Technol. **21**, 094034 (2010).